Geochemical variations at ridge-centered hotspots caused by variable melting of a veined mantle plume

Todd Anthony Bianco [a,*], Garrett Ito [b], Jeroen van Hunen [c], John J. Mahoney [b,1], Maxim D. Ballmer [b]

[a] Geological Society of America—United States Geological Survey Congressional Science Fellow, Washington, DC, USA
[b] Department of Geology and Geophysics, SOEST, University of Hawaii Manoa, Honolulu, HI 96822, USA
[c] Department of Earth Sciences, Durham University, Durham DH1 3LE, United Kingdom

ARTICLE INFO

ABSTRACT

We model the dynamics and melting of a ridge-centered mantle plume, and predict the geochemical composition of magma at the surface. The mantle source is a fine-scale mixture of a small fraction of hydrous peridotite that is relatively enriched in incompatible elements ("EC") and is embedded in a drier peridotite ("DC") matrix. We assume all magma erupts at the ridge and calculate the contribution of EC and DC to the pooled composition along the ridge. If viscosity increases as melting dehydrates the mantle, EC contributes more to the pooled magma at the hotspot center than anywhere else along the ridge. The magnitude of this EC anomaly increases with Rayleigh number, and the along-axis distance to normal ridge composition increases with Rayleigh number, plume radius, and thermal buoyancy flux. A subset of model calculations designed to simulate the Iceland hotspot and Mid-Atlantic Ridge predict variations in crustal thickness, $^{87}Sr/^{86}Sr$, and La/Sm with magnitudes and widths along the ridge that are comparable to, but less than, those observed. Improved fits to the observations require the innermost plume mantle to be compositionally distinct from the ambient asthenosphere; for example, by having a slightly higher mass fraction of EC (13–16%), or with DC having slightly higher $^{87}Sr/^{86}Sr$ and La/Sm. The inferred bulk plume $^{87}Sr/^{86}Sr$ composition, however, is within the predicted range of the source of normal mid-ocean ridge basalts worldwide. The broader implication is that the source of the Iceland plume is more similar in composition to the ambient upper mantle than previously thought, as a large part of the variation in ridge basalt composition can be attributed to the dynamics of mantle flow and melting.

1. Introduction

The largest variations in the composition and thickness of crust along mid-ocean ridges are often attributed to the interactions of ridges with mantle plumes (e.g., Hart et al., 1973; Ito et al., 2003; Morgan, 1972; Schilling, 1973; Vogt, 1971; Wilson, 1963). For example, Iceland has an extremely thick crust (up to ∼40 km, Darbyshire et al., 1998) and the thickness decreases with distance to the north and to the south along the Mid-Atlantic Ridge (MAR) (e.g., Hooft et al., 2006; Menke, 1999; Smallwood et al., 1995; Weir et al., 2001) to values (∼7 km) that are within the range found at ridges not influenced by mantle plumes (e.g., Dick et al., 2003; White et al., 1992). Local seismic tomography studies have imaged the Iceland mantle plume as a columnar-shaped body with low seismic wave speeds in the upper mantle beneath Iceland

(e.g., Allen et al., 2002; Hung et al., 2004; Wolfe et al., 1997), and geodynamic models have shown how a plume with a diameter comparable to that (∼200 km) of the seismic velocity anomaly can successfully explain the variations in crustal thickness observed at Iceland and along the MAR (Ito et al., 1999). Geochemical studies have shown evidence for anomalously rapid upwelling beneath Iceland (Maclennan et al., 2001; Peate et al., 2001), in further support of a buoyantly rising mantle plume.

Accompanying the anomaly in crustal thickness are anomalously high $^{206}Pb/^{204}Pb$, $^{87}Sr/^{86}Sr$, $^{3}He/^{4}He$, and La/Sm and low $^{143}Nd/^{144}Nd$, as well as additional compositional anomalies, which change gradually with distance from Iceland (e.g., Cohen and O'Nions, 1982; Hanan and Schilling, 1997; Hart et al., 1973; Hemond et al., 1988; Mertz et al., 1991; O'Nions et al., 1973; Schilling, 1973; Schilling et al., 1999; Wood et al., 1979; Zindler et al., 1979). Like crustal thickness, the geochemical anomalies are largest on Iceland and diminish with distance north and south along the MAR to values more typical of normal mid-ocean ridges.

A common interpretation of the geochemical variations is that they reveal an Iceland mantle plume that is compositionally

---

distinct from, and is becoming more diluted as it mixes with the ambient mantle with distance away from Iceland (e.g., Schilling, 1973, 1991). The main difficulty with this interpretation is that previous geodynamic models of a mantle plume rising beneath a mid-ocean ridge fail to predict significant mixing between material native to the plume and material native to the ambient upper mantle (Ito et al., 1999). Thus, rather than along-axis gradients in composition, previous numerical models have predicted a more-or-less uniform composition along the whole section of the ridge influenced by the plume, and a step-like change to normal ridge compositions outside of this section (Ito et al., 1999). Alternatively, the Iceland mantle plume may have some form of radial zoning in composition on the regional scale, for example, due to the entrainment of ambient mantle as it rises from the lower mantle (e.g., Hauri et al., 1994). However, geodynamic models that simulate such a process predict little or no mixing between the hot center of a plume and the surrounding, entrained material (Farnetani and Richards, 1995). This prediction complicates an explanation for the gradual changes in compositions with distance away from central Iceland.

A possible solution may be related to how different mantle materials are extracted by melting in response to variations in mantle flow. One key concept is that upwelling and decompression melting in a mantle plume tends to be faster near the base of the melting zone than near the top, and this leads to melt compositions heavily concentrated in incompatible elements (Maclennan et al., 2001), i.e., those elements that are extracted near base of the melting zone. But in addition, if the mantle is composed of a mixture of enriched material that is more fusible than accompanying depleted material, the rapid deep upwelling of plumes can lead to a greater concentration of the enriched components in the melts than in starting mantle source (Ito and Mahoney, 2005a, 2005b). A number of studies have argued that both "enriched" materials (e.g., high $^{87}Sr/^{86}Sr$) as well as "depleted" materials (e.g., low $^{87}Sr/^{86}Sr$) are intrinsic to the Iceland plume (e.g., Breddam, 2002; Hards et al., 1995; Fitton et al., 1997; Thirlwall et al., 2004) (although this point is still debated (Hanan et al., 2000; Mertz and Haase, 1997; Stracke et al., 2003)). Geodynamic models that assume such compositional heterogeneity is present at the fine scale ($\leq \sim 10^\circ$ km, e.g., a "veined" mantle) in plumes at intraplate (Bianco et al., 2005, 2008, 2011) as well as near-ridge settings (Ingle et al., 2010; Ito and Bianco, in press) have demonstrated that spatial variations in upwelling and melting rates can give rise to gradients in magma composition at the surface. Such a process may be occurring beneath the MAR near Iceland.

Here we test the hypothesis of variable melt extraction from a veined mantle using geodynamic models that simulate 3D upper mantle flow, heat transfer and melting of a ridge-centered plume. Our overarching goal is to quantify, generally, the degree to which flow and melting of a heterogeneous mantle can influence the variability in magma composition along a plume-influenced ridge axis. The effects of temperature- versus compositionally-dependent mantle rheology, radius of the plume thermal anomaly, and reference viscosity of the mantle are quantified. Finally, we compare predictions to observations of $^{87}Sr/^{86}Sr$, the incompatible element ratio La/Sm, and crustal thickness along the Iceland–MAR system.

2. Methods

We simulate upper mantle convection of an incompressible, infinite-Prandtl-number fluid with CITCOM, a Cartesian coordinate finite-element code (Moresi and Gurnis, 1996; van Hunen et al., 2005; Zhong et al., 2000). For the energy equation, we use the extended Boussinesq approximation and account for cooling due to latent heat of melting and adiabatic decompression (see Appendix 1 of Bianco et al. (2011)). Melting is handled by using passive tracers to advect melt depletion and by using parameterizations of hydrous peridotite melting (Katz et al., 2003). The mantle in these models is uniformly heterogeneous (veined), and the heterogeneities are assumed to be in thermal equilibrium. For simplicity, chemical interaction between melt and solid are ignored, which is appropriate for fractional melting (e.g., Johnson et al., 1990; Kelemen et al., 1997; McKenzie, 2000; Rubin et al., 2005; Stracke et al., 2006; Zhu et al., 2011). More generally (e.g., if there is some melt–solid interaction), our treatment applies to a situation in which magmas from different components reach the surface in approximately the same relative proportion as they were formed by decompression melting. More details of the method are in Bianco et al. (2008, 2011). Unless otherwise noted in Supplementary Tables S1 and S2, melting parameters are the same as in Bianco et al. (2008, 2011) and Table 2 of Katz et al. (2003). The following section discusses the main adaptations for the current study.

### 2.1. Model setup, boundary, and initial conditions

The general model setup is shown in Fig. 1. All models include the upper 400 km of mantle (z-dimension), and $\geq$1600 km of ridge axis (y-dimension) and $\geq$800 km in the direction of plate motion (x-axis). Vertical resolution is 5 km at depths above 225 km, which provides adequate resolution in the melting zone; vertical resolution is $\leq$9 km below 225 km, and horizontal resolution is 6.25 km everywhere. To ensure a steady state, calculations were run for $\sim$100 Myr of model time.

As in the previous work (Bianco et al., 2008, 2011), the initial temperature condition is set using a half-space cooling model (Davis and Lister, 1974), and in all cases the initial thermal age at the ridge (x=0) is set to 0.01 kyr to allow the axial lithosphere to start with a finite thickness. A plume is imposed as a steady, hot circular patch at the base of the model (e.g., Bianco et al., 2008, 2011; Ribe et al., 1995). The anomaly is greatest at the center ($T_{plume}=200\,^\circ$C, at $(x,y)=(0,0)$ km) and decays as Gaussian function of radial distance. The radius r_{plume} is the distance at which the thermal anomaly has decayed by a factor of $1/e$. The rest of the model base is kept at the simulated ambient potential temperature of 1300 $^\circ$C (we include an adiabatic gradient). This potential temperature is near the lower bound of recent estimates for normal upper mantle (e.g., Putirka, 2005; Herzberg et al., 2007; Lee et al., 2009) and leads to predicted crustal thicknesses (4–5 km) in models without a plume—at the low end of the range observed at the relevant half spreading rate (10 km/Myr) (Brown and White, 1994; White et al., 1992; Dick et al., 2003). The main reason for using this temperature is computational advantages; the shallower solidus allows for higher resolution in the melting zone at a given computational expense.

Plate motion is simulated with a horizontal velocity in the x direction of 10 km/Myr (i.e., approximately the half-spreading rate near Iceland (DeMets et al., 2010)) imposed on the top of the model space. The vertical walls beneath the ridge (x=0) and slicing through the center of the hotspot (y=0) are reflecting, insulating boundaries, and are thus planes of symmetry. All other boundaries are open to material flow with zero conductive heat flow. Thus, the symmetry of the problem allows us to simulate one quarter of the full volume of a ridge-centered plume system.

2.2. Rheology

Viscosity η is controlled by temperature-dependent Newtonian rheology with an additional term to simulate the stiffening of the
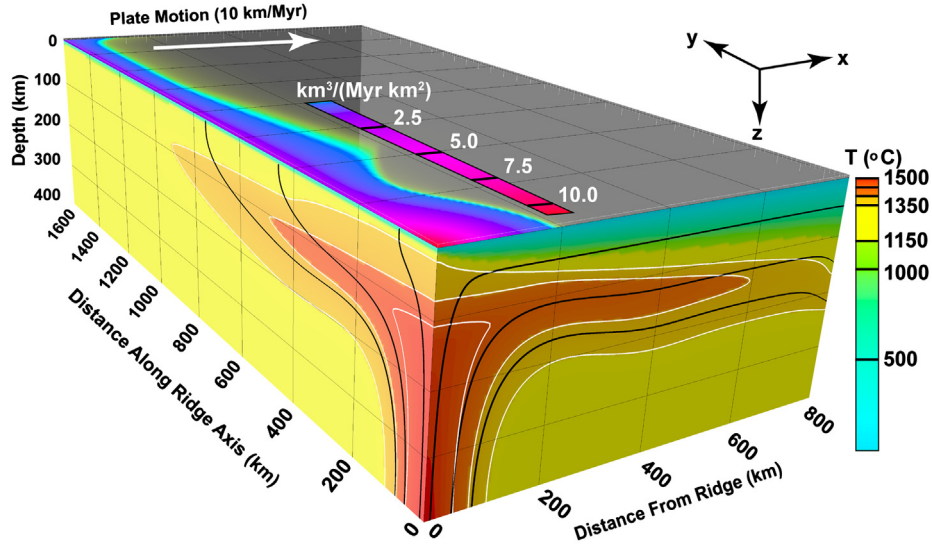
Fig. 1. Vertical slices through an example model domain show projections of the 3D potential temperature in shades of blue (warm) to red (hot). Total depth (z-axis) of simulation is 400 km and horizontal dimensions are 1600 km along the ridge axis (y-axis), and 800 km in the direction of plate motion ("distance from ridge"; x-axis). Black lines are streamlines and white lines mark potential temperatures of 1350 °C, 1400 °C, and 1450 °C. The total flux of vertically transported melt is contoured on the horizontal surface and is ∼5 times greater over the center of the thermal plume. We model a veined mantle that is 90% anhydrous peridotite ("DC") and 10% hydrous peridotite ("EC"). Viscosity only depends on temperature, not water content, in the case shown. (For interpretation of the references to color in this figure legend, the reader is referred to the web version of this article.)

mantle due to the extraction of a small amount of water by modal partial melting (Hirth and Kohlstedt, 1996, 2003),

$$\eta = \eta_0 \left(\frac{C_s^w}{C_0^w}\right)^{-r} \exp\left[\frac{E_a}{R}\left(\frac{1}{T} - \frac{1}{T_{ref}}\right)\right] \tag{1}$$

where η_0 is the reference viscosity, E_a is the activation energy, R is the gas constant, T is absolute temperature, and T_{ref} is absolute reference temperature. This equation has a standard Arrhenius dependence on temperature (see Table 1 for definition and values of variables) and has viscosity decreasing exponentially (with coefficient r) with the ratio of water concentration in the solid residue C_s^w relative to the starting concentration C_0^w prior to melting. The activation energy used ($E_a = 120$ kJ/mol) is lower than values measured in laboratory experiments to simulate the effects of power-law rheology (Christensen, 1984; Watts and Zhong, 2000).

Eq. (1) is incorporated with the following adaptations needed to simulate melting of two mantle components with different water contents. Assuming modal fractional melting, the water content of the solid changes with extent of melting F from its initial value C_0^w according to (Shaw, 1970)

$$C_s^w = C_0^w(1-F)^{1/D-1} \equiv C_0^w \beta(F), \tag{2}$$

where D is the bulk distribution coefficient, for which we assume $D = 0.01$ (Michael, 1995). The function $\beta(F)$ describes the solid's depletion of water content relative to its original concentration. A function that describes the water-dependence of viscosity of mantle component n is therefore

$$\mu_n = ({}^nC_0^w \beta n(F))^{-r} \tag{3}$$

The net effect on the viscosity of a system with two components that are present in volumes smaller than the control volume of the continuum is

$$\frac{1}{\mu_{eff}} = \frac{\phi_1}{\mu_1} + \frac{\phi_2}{\mu_2} \tag{4}$$

where ϕ_n is the mass fraction of component n. With the water-dependence of each component described by (3), Eq. (4) becomes

$$\frac{1}{\mu_{eff}} = ({}^1C_0^w \beta_1)^{-r}\phi_2 + \frac{({}^2C_0^w \beta_2)^{-r}\phi_1}{({}^1C_0^w \beta_1 \, {}^2C_0^w \beta_2)^{-r}}, \tag{5}$$

Normalizing (5) by its value prior to melting (i.e., when $\beta_n(0) = 1$), the dimensionless function is

$$\mu'_{eff} = \frac{\mu_{eff}}{\mu_{eff}(F=0)} = (\beta_1\beta_2)^{-r}\left[\frac{({}^1C_0^w)^{-r}\phi_2 + ({}^2C_0^w)^{-r}\phi_1}{({}^1C_0^w \beta_1)^{-r}\phi_2 + ({}^2C_0^w \beta_2)^{-r}\phi_1}\right] \tag{6a}$$

When $F_n = 0$, $\mu'_{eff} = 1$, but as $F_n \to 1$, $\mu'_{eff} \to \infty$; therefore we limit the maximum amount that dehydration can increase the viscosity,

$$1 \le \mu'_{eff} \le \mu'_{lim} \tag{6b}$$

with the reference value of μ'_{lim} being set to 100 (Hirth and Kohlstedt, 1996, 2003). Thus, the non-dimensional dynamic viscosity simulated in the numerical models is

$$\eta' = \frac{\eta}{\eta_0} = \mu'_{eff}\exp\left[\frac{E_a}{T_{ref}R}\left(\frac{1}{T'}-1\right)\right] \tag{7}$$

where T' is the non-dimensional absolute temperature. Therefore, (6,7) state that unmelted mantle (i.e., $F = 0$ for all components) at the ambient reference temperature has a scaled viscosity of $\eta' = 1$. In model simulations, we set the Rayleigh number, Ra, which in turn sets the dimensional reference viscosity η_0 (1). Because μ'_{eff} is normalized by μ_{eff} prior to melting and limited by μ'_{lim}, the absolute water content does not affect the reference viscosity (or Ra), but does affect at what depth (more water leads to a deeper solidus), how much, and how quickly viscosity increases with melting and dehydration. This formulation is advantageous in allowing us to easily examine the effects of varying Ra ($\sim 1/\eta_0$) and initial water content separately.

2.3. Geochemistry and crustal thickness

The isotopic composition and the thickness of the crust are computed by assuming that modal fractional melting controls the elemental concentrations in the magma and that all magma

Table 1
General constants and variables.

Symbol	Meaning	Value	Units
B	Buoyancy flux		Mg/s
${}^nC_0$	Concentration of incompatible element in initial solid component n		ppm
${}^nC_0^w$	Concentration of water in initial solid component n	1–400	ppm
D	Bulk partition coefficient		[a]
DC	"Depleted Component"		
$E(F)$	Enrichment function of incompatible element in the melt for modal fractional melting		[a]
E_a	Activation energy	1.20×10^5	J/mol
EC	"Enriched Component"		
F^n	Fraction melt depletion of component n		[a]
h_c	Crustal thickness along ridge axis		km
I^n	Isotope ratio of component n		[b]
I_R	Isotope ratio of pooled magma along the ridge axis ("EC fraction")		[a]
ΔI_R	Difference between EC fraction at the plume center and normal ridge		[a]
$\dot{M}$	Melting rate		%/Myr
r	Coefficient of dehydration term in viscosity	1–1.5	[a]
R	Gas constant	8.314	J/(mol K)
Ra	Rayleigh number	2.6×10^4–1.3×10^6	[a]
r_{plume}	Radial scale of plume thermal anomaly	75–225	km
T	Absolute temperature		°C
T'	Non-dimensional absolute temperature		[b]
T_{plume}	Maximum thermal anomaly	200–225	°C
T_{ref}	Reference temperature	1300	°C
u_{plate}	Plate velocity	10	km/Myr
x,y,z	Cartesian coordinates, in direction of plate motion, perpendicular to plate motion, depth	0–800, 0–3200, 0–400	km
Δy_{min}	Along axis distance to minimum I_R		km
Δy_{norm}	Along axis distance to normal-ridge I_R		km
$\beta(F)$	Depletion function of an incompatible element in the source for modal fractional melting		
η	Dynamic viscosity		Pa s
η_0	Reference viscosity	1.1×10^{20}–4.2×10^{21}	Pa s
η'	Non-dimensional viscosity		[b]
μ	Dehydration function term in viscosity		[b]
μ_{eff}	Effective dehydration function for two component mixture		[b]
μ_{eff}'	Normalized μ_{eff}		[b]
μ_{limit}'	Imposed maximum of μ_{eff}'		[b]
ρ_c	Crust density	2800	kg/m³
ρ_m	Mantle density	3300	kg/m³
ϕ_n	Mass fraction of component n		[b]

[a] Denotes naturally dimensionless quantity.
[b] Denotes non-dimensionalized quantity.

liberated in the mantle rises to the surface and forms the crust. The isotope ratio I_R at a given position of the ridge axis is computed by summing the contributions from the magma generated in each vertical plane of the model perpendicular to the ridge axis,

$$I_R = \frac{\Sigma_{n=1}^2 I^n \phi_n {}^nC_0 \int_x \int_z E_n(F)\dot{M}_n dz dx}{\Sigma_{n=1}^2 \phi_n {}^nC_0 \int_x \int_z E_n(F)\dot{M}_n dz dx} \qquad (8)$$

where I^n is the isotope ratio of component n; ${}^nC_0$ is the initial concentration of an incompatible element in component n; $\dot{M}_n(\geq 0)$ is the local melting rate of component n; and $E_n(F)$ is the enrichment of an incompatible element in modal fractional melts from component n relative to the solid. In simulations with $I^{EC}=1$ and $I^{DC}=0$, I_R is equal to the "EC fraction", or the fractional contribution of EC to the incompatible-element composition of the pooled magma.

Crust is accumulated along the ridge, where crustal thickness of pooled magma is

$$h_c = \frac{\rho_m}{\rho_c} \frac{1}{u_{plate}} \sum_l^2 \phi_n \int_x \int_z \dot{M}_n dz\, dx \qquad (9)$$

where ρ_m and ρ_c are mantle and crust density (3300 and 2800 kg/m³, respectively) and u_{plate} is the half spreading rate of the ridge.

3. Simulations of ridge-centered plumes

This section discusses how key characteristics of an along-axis geochemical anomaly (e.g., amplitude and wavelength) depend on the dynamics of a ridge-centered mantle plume. In each simulation, there are two peridotite components with different water contents. One component ("DC") is a "depleted" peridotite in that it has experienced relative depletion of incompatible trace elements over a long timescale, and has relatively low water content. The other component ("EC") is a relatively "enriched" peridotite. DC is arbitrarily assumed to be 90% of the starting solid ($\phi_{DC}=0.9$) and EC 10% ($\phi_{EC}=0.1$), and unless otherwise noted, the initial water content of DC and EC is 1 ppm and 400 ppm, respectively. The starting concentration of an incompatible element, C_0, in (8), and its bulk partition coefficient ($D=0.01$), are the same for both components. Also, the bulk partition coefficient of water ($D=0.01$) is the same for both components in (6). Finally, in Eq. (8), $I^{DC}=0$ and $I^{EC}=1$ so that I_R equals the "EC fraction" as described above.

3.1. Effects of water-dependence of viscosity

Fig. 2a shows the fraction of EC in the incompatible element composition along the ridge (I_R; (8)) for simulations in which viscosity depends on both temperature and water (the exponent in Eqs. (5) and (6) is $r=1$, and $\mu_{lim}=100$), and another in which viscosity depends on temperature only and not water ($r=0$). In

both simulations, I_R is relatively high over the center of the plume and decreases along the ridge to the sides of the plume. I_R gradually increases at an along-axis distance from the plume of $y \sim 350$ km in the case in which viscosity is temperature-dependent only, and $y \sim 600$ km in the temperature and water-dependent case. EC fraction eventually levels off to the "normal" ridge value of ~ 0.15 farther away from the plume. At $y \sim 1400$–1600 km along the ridge axis, both simulations are influenced by boundary effects that are artifacts of the model design and therefore will be ignored in the discussion below.

We use three key measurements to characterize the predicted geochemical anomaly caused by plumes. The first is the difference between I_R directly above the plume center and above the normal section of ridge, ΔI_R (Figs. 2a and 3b). Another measurement is the along-axis distance to the minimum I_R, Δy_{min} (Figs. 2a and 3b). Finally, we measure the along-axis distance to the normal-ridge composition, Δy_{norm} (Figs. 2a and 3b). Thus, we will discuss a short-wavelength (Δy_{min}) and long-wavelength (Δy_{norm}) geochemical anomaly caused by the plume.

In both models shown in Fig. 2, the local high and associated decrease in I_R away from the plume center (between 0 and 200 km) arises from the rapid buoyant upwelling of plume mantle

within the plume stem: the closer to the plume center, the greater the flux of material through the base of the melting zone, and this causes EC to melt more voluminously nearer the plume center. However, it is important to notice that ΔI_R is positive (i.e., I_R is greater over the plume center than at the normal ridge) only in the case with water-dependent viscosity. Without water-dependence, the buoyancy-driven upwelling enhances the melting of both EC and DC, therefore the composition above the plume is similar to that far from the plume. With water-dependent viscosity, buoyancy-driven mantle upwelling enhances melting of EC more than DC; mantle flow and decompression melting in the stiff, dehydrated DC melting zone is relatively slow, and is driven primarily by plate spreading (Fig. 2b and d).

Beyond ~ 200 km EC fraction continues to decrease to the measured Δy_{min} for two reasons: away from the plume center, (1) the flow becomes more horizontal, and vertical velocity as well as melting rate decrease, especially where EC melting is liberating incompatible elements, and (2) previously melted material that is depleted of incompatible elements has been diverted laterally and continues to melt in this region. Both effects are greater in the case with (only) temperature-dependent viscosity. Fig. 2c and e shows mantle flow streamlines, velocity vectors, and the 0.05%/Myr
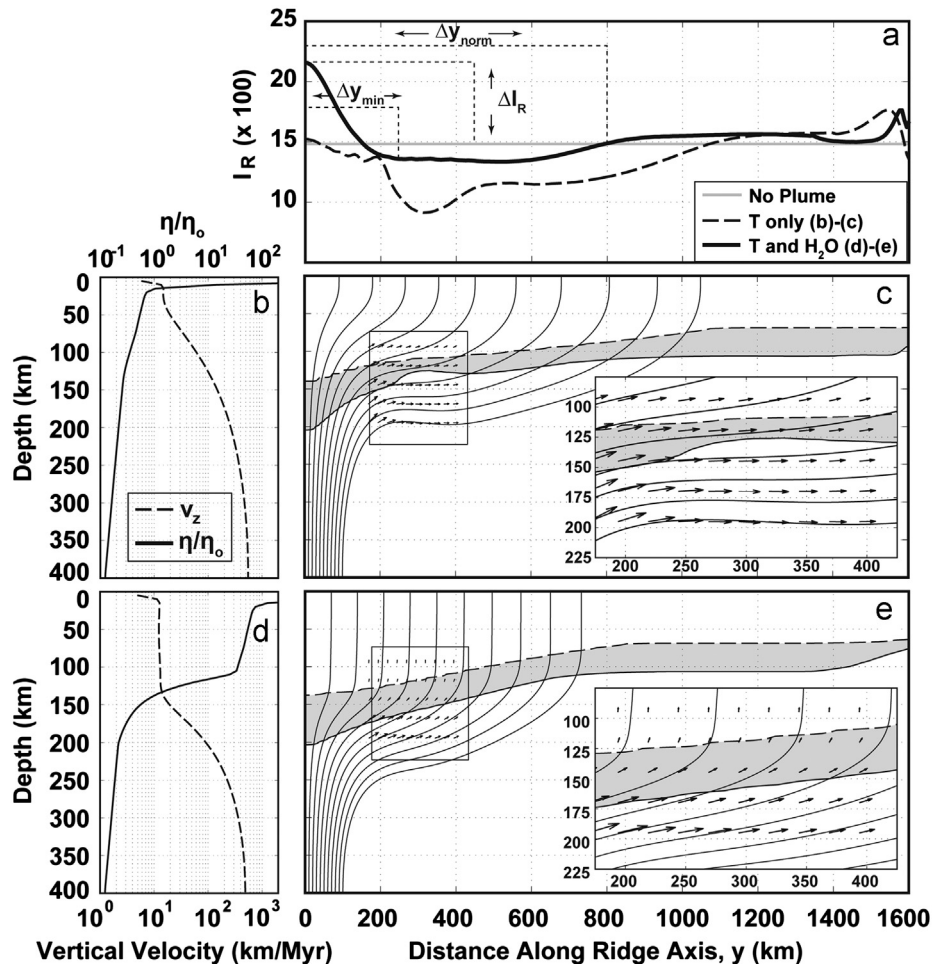
Fig. 2. (a) Fraction of pooled magma derived from EC (or I_R because $I^{EC} = 1$ and $I^{DC} = 0$) versus distance along the ridge (y-axis) from the center of the plume ($y = 0$). Case in which viscosity depends only on temperature is simulated by $r = 0$ in Eq. (1) (dashed black line); cases in which viscosity also depends on water content is simulated by $r = 1.0$ (solid black line); case with no plume and $r = 1.0$ (solid gray line). The height of the geochemical anomaly over the plume center is ΔI_R, the distance to the minimum EC fraction (the width of the short-wavelength anomaly) is Δy_{min}, and the distance to normal-ridge composition (the width of the long-wavelength anomaly) as Δy_{norm} (marked for the case plotted as a solid black line). (b) Non-dimensional mantle viscosity (solid line, top horizontal axis) and vertical velocity (dashed line, bottom horizontal axis) versus depth, at the plume center (i.e., $x = 0$, $y = 0$) for the simulation in which rheology depends on T only (i.e., $r = 0$). (c) Thin lines are solid material streamlines (streamlines are 2D along the y-axis because of the boundary conditions). Gray region is the area in which EC melting rate is $> 0.05\%$/Myr and DC is not melting; both components melt above the dashed line (contour of 0.05%/Myr EC melting rate). Inset shows a magnification of the boxed area. Arrows are solid velocity vectors with length proportional to speed. (d) Same as (b), but for the simulation in which $r = 1$. (e) Same as (c), but for the simulation in which $r = 1$.
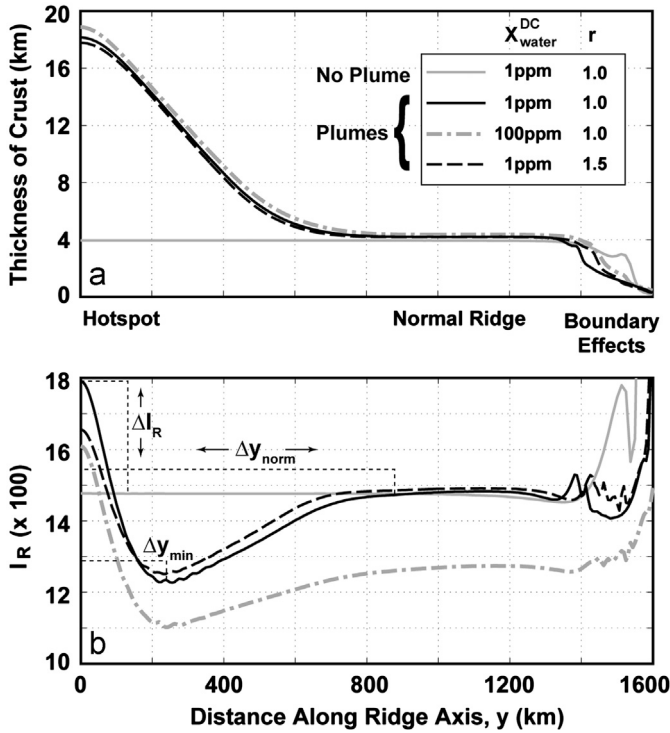
Fig. 3. Crustal thickness (h_c; Eq. (9)) along the ridge axis for a simulation with no plume (solid gray line), a simulation in which $^{DC}C_0^w = 1$ ppm and $r = 1.0$ (solid black line), a simulation in which $^{DC}C_0^w = 1$ ppm and $r = 1.5$ (dashed black line), and a simulation in which $^{DC}C_0^w = 100$ ppm and $r = 1.0$ (dash–dotted gray line). $^{EC}C_0^w = 400$ ppm in all cases. Large variations within ∼200 km of the (right) end of the model box are boundary artifacts and should be ignored. (b) EC fraction (I_R; Eq. (8)) of an incompatible element in pooled magmas along the axis for the same simulations as in (a). ΔI_R, Δy_{min}, Δy_{norm} are marked with dotted lines.

melting rate contours of the EC and DC melting zones. In the region below the local minima in I_R ($y \sim \Delta y_{min}$) the vertical velocity component is smaller, and the lateral transport is greater in the temperature-only case compared to the case with the additional water-dependence. Thus the overall effects of dehydration are to cause a positive ΔI_R and keep I_R closer to normal ridge values beyond the sides of the plume stem.

Further from the center at $y = \Delta y_{norm}$, I_R levels out at the composition of the normal model ridge ($I_R \sim 0.15$) where there is no excess plume temperature or buoyant flow. This marks the longest-wavelength influence of the plume on the ridge.

3.2. Effects of the water-dependence exponent "r"

Fig. 3 shows crustal thickness (h_c; (9)) and composition along the ridge for simulations in which the exponent in (6a) $r = 1.0$ and 1.5; a range allowed by the results of laboratory experiments (Hirth and Kohlstedt, 2003). We also include a "normal-ridge" simulation without a plume and $r = 1.0$. In all three cases, $^{DC}C_0^w = 1$ ppm and $^{EC}C_0^w = 400$ ppm as they were for the reference case presented in the previous section.

The case with greater r has a smaller ΔI_R because the difference in vertical velocity between the base of the EC and DC melting zones is smaller (Fig. 4a and b), allowing for less EC, relative to DC melting. This effect on vertical velocity is primarily caused by a greater r leading to more rapid stiffening of the mantle at the base of the EC melting zone. This same effect slightly reduces h_c above the center of the plume in the case with greater r. Varying r has no discernable effect on Δy_{min} in these simulations; however, the case with larger r has a smaller Δy_{norm} because the lateral transport of plume material is also reduced.

3.3. Effects of DC water content

Crustal thickness and composition are also shown (Fig. 3) for a simulation in which $^{DC}C_0^w = 100$ ppm. More water in DC leads to a lower I_R everywhere along the ridge because the DC melting zone is thicker. ΔI_R is slightly larger in this particular simulation with more water, but this trend is reversed in other simulations, as adding even more water to DC eventually causes it to melt more similarly to EC, and thus I_R tends toward a uniform value of ϕ_{EC}. Finally, the along-axis distance to normal ridge composition (Δy_{norm}) is larger in the case with greater water content because viscosity is less sensitive to EC dehydration if DC also has high water content (see (5)), and so the plume spreads farther along the ridge axis (Fig. 4b).

### 3.4. Effects of reference viscosity on ridge composition

In the present model, Ra defines reference viscosity, η_0, and controls the vigor of convection and lateral variations in flow rate. To examine the effects of the spatial variations in mantle velocity, we first examine cases in which η_0 is varied, but the thermal buoyancy flux is approximately preserved. Here we compensate for the effects of different η_0 by varying the radius of the plume, r_{plume} (see Fig. 5a and b for values of η_0 and r_{plume}).

Simulations with smaller η_0 result in larger ΔI_R (Fig. 5b) because these cases have significantly larger vertical velocities at a given depth below the DC solidus, but have approximately the same vertical velocity above the DC solidus, where again, upwelling is controlled primarily by plate spreading (see the inset of Fig. 5a). Similarly, cases with smaller η_0 predict that h_c is larger because of increased melt production at the base of the EC melting zone. The predicted increase in the long-wavelength distance of plume influence (Δy_{norm}) supports findings of prior studies that show decreasing reference viscosity increases the distance plume material travels along the ridge axis for a given buoyancy flux (e.g., Ribe et al., 1995).

For cases in which buoyancy flux is allowed to change with η_0 because r_{plume} is fixed (Fig. 5c), the changes in geochemical anomalies with η_0 are qualitatively similar to those cases in which buoyancy flux was preserved (Fig. 5b). The main difference is that Δy_{norm} is more sensitive to η_0 than in the cases above, because when holding r_{plume} constant, decreasing η_0 also leads to greater buoyancy fluxes. An increase in plume width with buoyancy flux is also well documented in the literature (Feighner and Richards, 1995; Ribe et al., 1995). Lastly, it is notable that the width of the short-wavelength geochemical anomaly, Δy_{min}, does not change significantly between the models examined here.

3.5. Effects of plume radius

The last set of experiments examines the effect of changing r_{plume} (values given in Fig. 6). With a constant η_0 (3.3×10^{20} Pa s), changing r_{plume} also changes buoyancy flux. Results show that crustal thickness (h_c) and ΔI_R are greater in cases with larger r_{plume}. ΔI_R increases with r_{plume} because the across-axis width (x-dimension) of the base of the two melting zones increases but the effect is greater for the EC melting zone than DC melting zone (DC is essentially dry in these cases), and hence proportionally more melts are derived from EC. The long-wavelength width of plume influence (Δy_{norm}) is controlled by the increase in plume waist width with volume flux (e.g., Ribe et al., 1995) as r_{plume} increases. In addition, Δy_{min} also increases with r_{plume} (Fig. 6b) because Δy_{min} is controlled by the along-axis width of the velocity anomaly associated with plume-stem upwelling, which increases with r_{plume}.
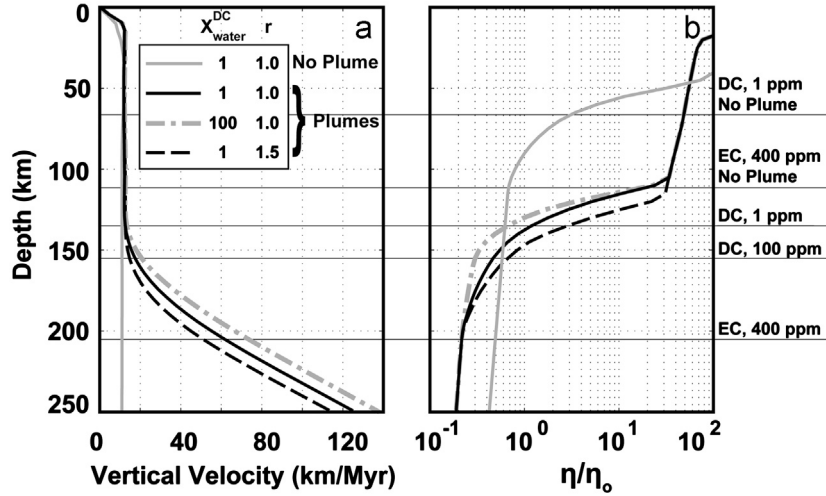
Fig. 4. (a) Vertical velocity versus depth in the upper 250 km of the model, and at the plume center ($(x,y)=(0,0)$) for the same simulations (and same line styles) as in Fig. 3. (b) Viscosity normalized by reference viscosity η_0 for the simulations in (a) and Fig. 3. Horizontal lines represent depths where EC and DC (with the noted water contents) begin melting with a 200 °C plume thermal anomaly. The solidi of EC with 400 ppm water and the DC with 1 ppm occur at shallower depths for a simulation with no plume, as noted in the figure.
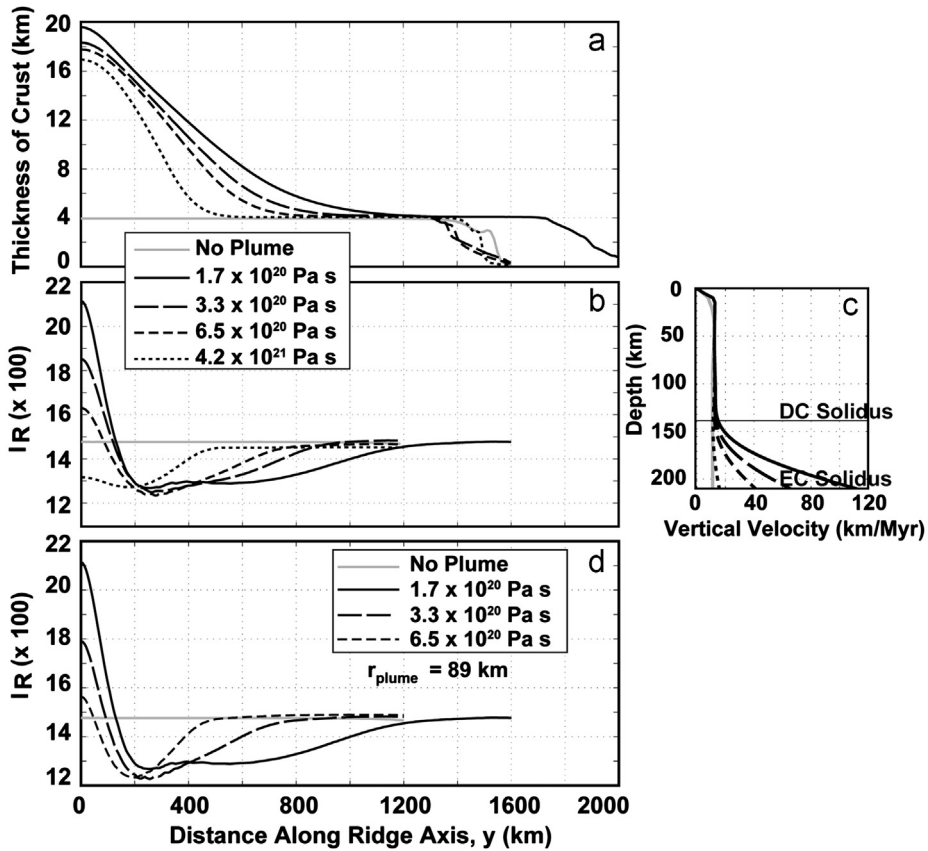
Fig. 5. (a) Crustal thickness and (b) EC fraction (I_R) along the ridge for cases with different η_0 as labeled but approximately the same plume buoyancy flux. The case without a plume has $\eta_0 = 1.7 \times 10^{20}$ Pa s. (inset) Vertical velocity versus depth in the upper 210 km of the model, and at the plume center ($(x,y)=(0,0)$). (c) EC fraction (I_R) for cases in which plume flux varies with η_0 (i.e., r_{plume} is fixed at 89 km). The case with no plume (black dash-dotted) is the same as that shown in (a).

3.6. Widths and magnitudes of predicted geochemical anomalies

To summarize our results for Sections 3.4–3.5, we show how ΔI_R, Δy_{min}, and Δy_{norm}, relate to plume buoyancy flux, B (Fig. 7). Buoyancy flux is an important quantity that may be estimated with geophysical observations and is widely used to characterize hotspots (e.g., Sleep, 1990). Fluid dynamic theory, laboratory experiments, and numerical model results all show that the total

width of plume influence (Δy_{norm}) increases with the square root of volume flux, which is directly proportional to buoyancy flux ($B^{1/2}$) (Feighner and Richards, 1995; Ribe et al., 1995). In our simulations we indeed find that a linear fit to Δy_{norm} versus $B^{1/2}$ has a correlation coefficient > 0.99 (Fig. 7a). The width of the high-EC fraction, short-wavelength anomaly, Δy_{min}, also increases linearly with $B^{1/2}$, but primarily through its sensitivity to r_{plume} rather than η_0 (i.e., Ra; Fig. 7b). Finally, the magnitude of the geochemical anomaly over
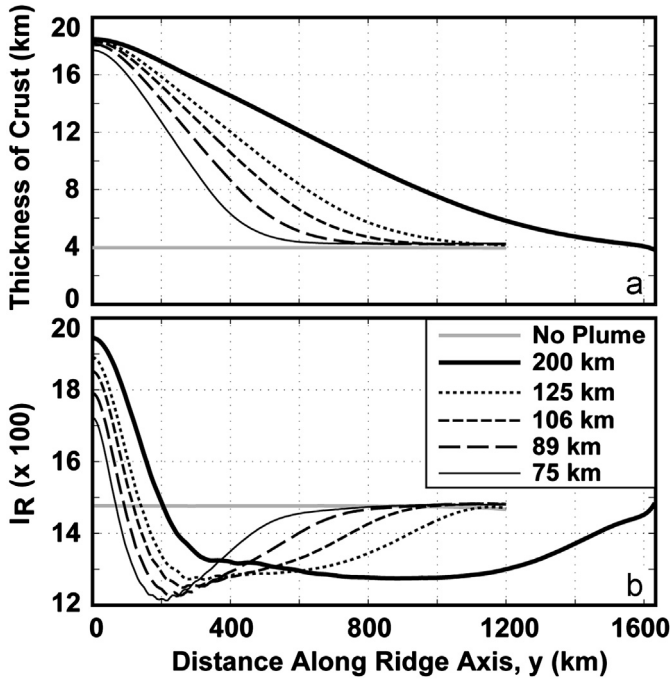
Fig. 6. (a) Crustal thickness for simulations with different r_{plume} and the same η_0. In the simulations $\eta_0 = 3.3 \times 10^{20}$ Pa s and $r_{plume} = 75$ km (thin solid line), 89 km (long-dashed line), 106 km (short-dashed line), 125 km (dotted line), and 200 km (thick solid line). We also include a case with no plume (solid gray line). The model space of the simulation in which $r_{plume} = 200$ km extends an extra 400 km along the ridge axis. Artifacts of the side boundary conditions exist but are not shown. (b) EC fraction (I_R) for the same simulations as in (a).

the center of the hotspot, ΔI_R increases primarily with Ra (or decreases with η_0) and secondarily with r_{plume} (Fig. 7c).

4. Comparisons with Iceland

4.1. Observations

We now explore which aspects of observed geochemical anomalies at Iceland these models can explain. We compare model predictions to observations of ^{87}Sr/^{86}Sr, crust thickness, and (La/Sm)$_{PM}$ (i.e., La/Sm relative to primitive mantle (Lyubetskaya and Korenaga, 2007)). We assume the plume is centered under Bárdarbunga Volcano (as in Ito et al. (1999)), which is consistent with the mantle seismic structure (Wolfe et al., 1997). In order to compare the simple geometry in the modeled ridge (straight and perpendicular to plate motion) to the geometry of the MAR near Iceland, we project data collected south of Bárdarbunga and north of 55°N to a line that passes through Bárdarbunga with an azimuth of 61°; this line represents the average trend of the Southwest Rift Zone on Iceland together with the Reykjanes Ridge. For the samples north of Bárdarbunga, positions are projected (east or west) to the nearest ridge segment. We then compute the absolute distances between Bárdarbunga and projected sample locations.

The results of these projections (e.g., Fig. 8a and c) are much like what has been shown in earlier studies (e.g., Hanan et al., 2000; Ito et al., 1999; Schilling, 1973). The plume influence is recognized as ^{87}Sr/^{86}Sr and (La/Sm)$_{PM}$ values (see Fig. 8 caption for data sources) that extend from low to high values within ~400 km of the plume center. Outside of the hotspot influence the compositions are restricted to relatively low values, except for another local high in ^{87}Sr/^{86}Sr and (La/Sm)$_{PM}$ evident near Jan Mayen Island to the north, which we disregard in this study as it

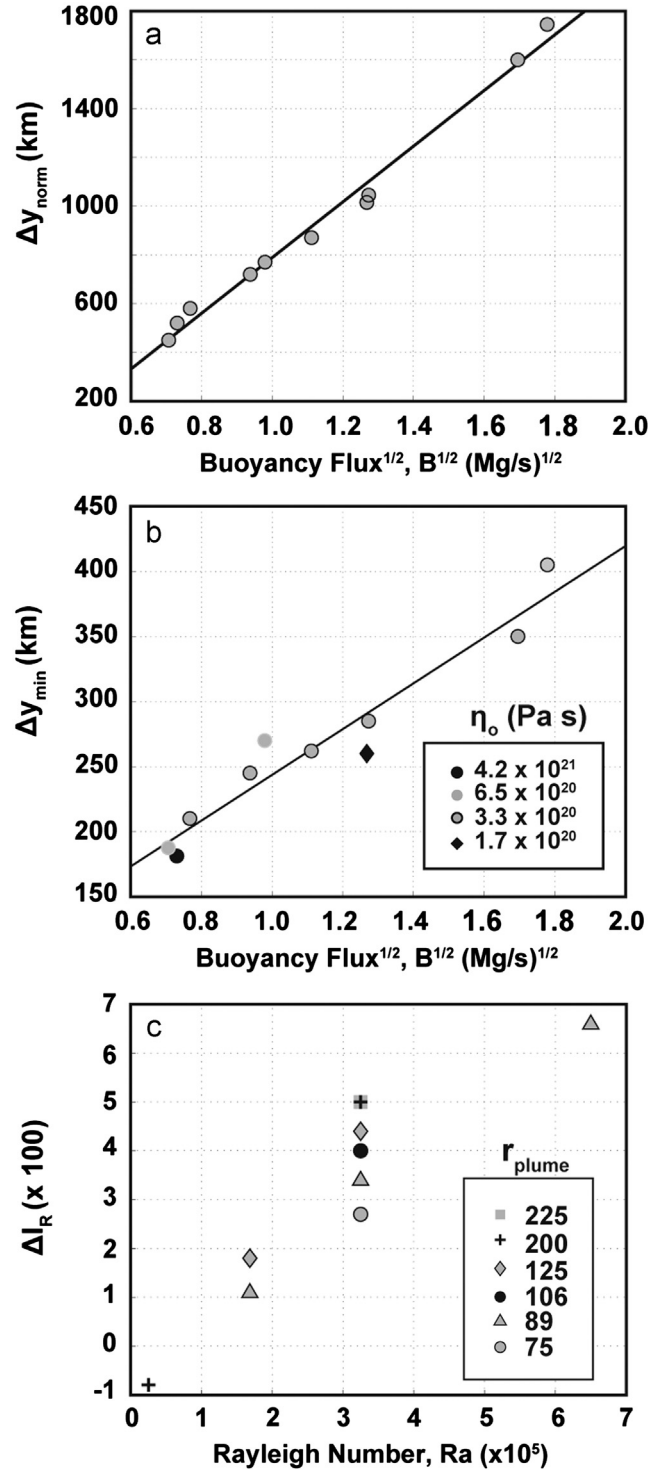**Fig. 7.** (a) Width of plume influence (Δy_{norm}; see Fig. 3b) versus the square root of thermal buoyancy flux ($B^{1/2}$) for models with $r = 1.0$, $^{DC}C_0^w = 1$ ppm, 1.7×10^{20} Pa s $< \eta_0 < 4.2 \times 10^{21}$ Pa s and 75 km $< r_{plume} < 225$ km. (b) Distance to the minimum EC fraction (Δy_{min}; see Fig. 3b) versus $B^{1/2}$ for the same simulations as in (a). Symbols distinguish different values of η_0 as labeled. The linear fits in (a) and (b) (black lines) have correlation coefficients of > 0.99 and > 0.96, respectively. (c) Magnitude of the geochemical anomaly (relative to normal-ridge composition of ~0.15) at the center of the hotspot (ΔI_R; see Fig. 3b) versus Rayleigh number Ra. Symbols distinguish different values of r_{plume} as labeled.

probably represents a separate hotspot from Iceland (e.g., Schilling et al., 1999).

As our models assume all melts generated in planes perpendicular to the ridge mix perfectly, the models only address changes
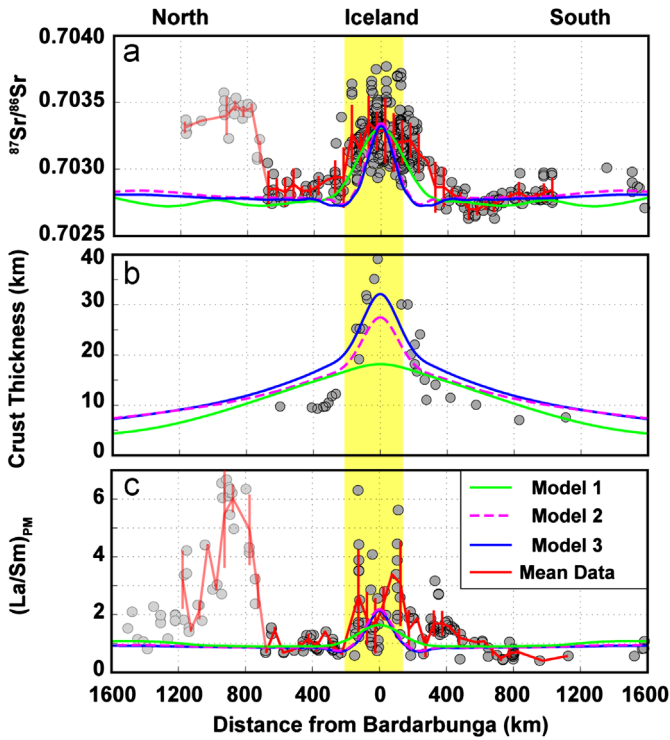
Fig. 8. Observations (circles) compared to model predictions (Model 1 is the green line; Model 2 is the magenta, dashed line; Model 3 is the blue line, parameters are described in the text and given in Supplementary Tables 1 and 2). (a) $^{87}Sr/^{86}Sr$ (gray circles) at Iceland (Cohen and O'Nions, 1982; Elliot et al., 1991; Hards et al., 1995; Hart et al., 1973; Hemond et al., 1988, 1993; Kokfelt et al., 2006; Mertz et al., 1991; Mertz and Haase, 1997; Murton et al., 2002; O'Nions and Parkhurst, 1974; O'Nions et al., 1976; Schilling et al., 1999; Stecher et al., 1999; Sun and Jahn, 1975; Taylor et al., 1997; White and Schilling, 1978; Wood et al., 1979; Zindler et al., 1979). To indicate two types of central values, the median of data grouped in 50 km intervals is shown (red line) with the standard deviation about the mean for each interval (red bars). (b) Crustal thickness; data (gray circles) are digitized from Hooft et al. (2006). (c) $(La/Sm)_{PM}$ (relative to primitive mantle (Lyubetskaya and Korenaga, 2007)); data from tholeiites sampled near Iceland (Hart et al., 1973; Schilling, 1973; Schilling et al., 1983, 1999; Hemond et al., 1993). Median values (red line) and standard deviations about the mean (red bars) are computed as described for (a). Yellow shadings indicate the north–south extent of subaerial Iceland. (For interpretation of the references to color in this figure legend, the reader is referred to the web version of this article.)

in mean composition, not the variability at a given location of the ridge axis. We therefore compute running means of the data in 50 km bins of distance from the Bárdarbunga. These running means of $^{87}Sr/^{86}Sr$ and $(La/Sm)_{PM}$ peak near central Iceland and decrease along the MAR. Depending on how one chooses a reference value, the $^{87}Sr/^{86}Sr$ anomaly is 0.0004 to 0.0005 higher than normal values, occurring over a width of ~530 km to 825 km; the $(La/Sm)_{PM}$ anomaly is 3.4–3.8 higher than normal values, occurring over a width of 475–840 km. Crustal thickness estimates along the ridge axis have been compiled by Hooft et al. (2006) (Fig. 8b). These estimates show a peak ~40 km near central Iceland, and decreases in crustal thickness to < 10 km within ~350 km to the north and ~600 km to the south.

4.2. Models with a uniformly veined mantle and no regional-scale compositional zoning

Three example cases are compared to the data (Fig. 8). Model 1 is most similar to the simulations throughout Section 3: $r_{plume}=225$ km, $\eta_0=1.7\times10^{20}$ Pa s, $T_{plume}=200$ °C, $\mu_{lim}=100$, $^{DC}C_0^w=1$ ppm, $^{EC}C_0^w=400$ ppm (see Supplementary Tables 1 and 2 for reference model

parameters). Models 2 and 3 have $\mu_{lim}=25$; a bulk water content that is more realistic for NMORB, $^{DC}C_0^w=100$ ppm and $^{EC}C_0^w=400$ ppm (Hirth and Kohlstedt, 1996, 2003); and a narrower radius that is in better agreement with seismic tomography results, $r_{plume}=100$ km (Allen et al., 2002; Hung et al., 2004; Wolfe et al., 1997). Model 2 has $\eta_0=1.1\times10^{20}$ Pa s and $T_{plume}=200$ °C, whereas Model 3 has $\eta_0=1.4\times10^{20}$ Pa s and $T_{plume}=225$ °C. In all three models, $^{87}Sr/^{86}Sr$, [La], [Sm], and $(La/Sm)_{PM}$ are higher in EC than in DC (see Supplementary Table 1). The source compositions were guided by the characteristics of recognized mantle end-member materials (Willbold and Stracke's (2006) "EM" and Salters and Stracke's (2004) DM), but ultimately, the compositions of EC and DC were set based on the values that tended to maximize the predicted variations in $^{87}Sr/^{86}Sr$ and $(La/Sm)_{PM}$ along the ridge axis The calculations also include the effects of garnet–spinel transition (at a depth of 90 km) and the exhaustion of clinopyroxene as parameterized by Katz et al. (2003). These changes influence the bulk partition coefficients for Sr, La, and Sm (using those of Salters and Stracke (2004), Supplementary Table S2) as well as the fractional melting equation used (term $E^n(F)$ in (8)) (McKenzie and O'Nions, 1991; Ito and Bianco, in press). The exhaustion of clinopyroxene also reduces the rate of melt production per increment of decompression.

All three of the example simulations predict a short-wavelength high with total $^{87}Sr/^{86}Sr$ variation that is comparable to values of the binned data collected near Iceland. In the case of Model 1, the total width of the predicted short-wavelength high in $^{87}Sr/^{86}Sr$ of ~800 km is comparable to, but still less than, the upper estimate of the width of high $^{87}Sr/^{86}Sr$ delineated by the binned means along the MAR. In Models 2 and 3, the widths of the high $^{87}Sr/^{86}Sr$ anomaly are narrower than that of Model 1, both ~500 km, which is ~60% of our upper estimate of the observed width. At distances > ~400 km north and south of central Iceland the predictions of all three cases roughly match the observed $^{87}Sr/^{86}Sr$ compositions, except near the Jan Mayen hotspot. The minimum and maximum values of the model $^{87}Sr/^{86}Sr$ values are controlled primarily by our choice of $^{87}Sr/^{86}Sr$ compositions of EC and DC. These results show that for the total variation of the running mean $^{87}Sr/^{86}Sr$ anomaly to arise without any regional scale, compositional heterogeneity in the mantle requires an extremely high $^{87}Sr/^{86}Sr$ for EC of ~0.7080–0.7090. Such a high $^{87}Sr/^{86}Sr$ is characteristic of, but still less extreme than, the compositions found at the Samoan hotspot (Jackson et al., 2007).

Like the variation in Sr isotopes, the models also predict a short-wavelength peak in $(La/Sm)_{PM}$ above the center of the hotspot. All three cases under-predict the range in the running mean $(La/Sm)_{PM}$ observed along the MAR, with the smallest total variation occurring in Model 1. The difference predicted between high $(La/Sm)_{PM}$ above the center of the plume and low $(La/Sm)_{PM}$ far from the plume center can be increased by raising $^{EC}[La]_0$ or $^{DC}[La]_0$ (or decreasing $^{EC}[Sm]_0$ or $^{DC}[Sm]_0$). However, varying these concentrations to increase the predicted (relative) range in $(La/Sm)_{PM}$ simultaneously results in absolute $(La/Sm)_{PM}$ values that are much higher than observations. Finally, the width of the high $(La/Sm)_{PM}$ is 600 km in Model 1, and ~300 km in Models 2 and 3, which are significantly narrower than even our lower-bound of ~475 km, and much narrower than the upper-bound 800 km, estimated from running means along the MAR near Iceland.

Among the three simulations, Model 3 is favored for two reasons. First, the radius of the plume in Model 3 is most consistent with width of the mantle seismic anomaly beneath Iceland (e.g., Allen et al., 2002; Hung et al., 2004; Wolfe et al., 1997). Second, the predicted crustal thicknesses best match those of Iceland: the maximum thickness in Model 3 of about 80% (32 km) of the peak thickness on Iceland (40 km). The remaining key weaknesses are that the width of the short-wavelength high

in $^{87}Sr/^{86}Sr$ and both the amplitude and width of the short-wavelength high in $(La/Sm)_{PM}$ are less than what is observed.

4.3. Models with a regional scale, compositional zoned plume

To address these discrepancies, two additional models (Models 3.1 and 3.2) consider the possibility that the source material rising in the center of the mantle plume is compositionally distinct from that of the ambient mantle. Model 3.1 (and 3.2) is based on Model 3 above, except that within the core of the plume, $\phi_{EC}=13\%$ and $\phi_{DC}=87\%$ (and $\phi_{EC}=16\%$ and $\phi_{DC}=84\%$ in Model 3.2), whereas everywhere else $\phi_{EC}=10\%$ and $\phi_{DC}=90\%$ as in Model 3. Moreover, less extreme $^{87}Sr/^{86}Sr$ values are used for DC and EC in Models 3.1 and 3.2 than in Model 3 (see Supplementary Table 1).

We define the inner core of the plume as encompassing the area within the 1460 °C isotherm in the hot patch at the base of the model (a radius of ∼58 km). We use the steady state velocity fields and temperatures from Model 3 to track this material through the melting zone and compute melting rates.

The net result of this compositional zoning is to widen the predicted $^{87}Sr/^{86}Sr$ and $(La/Sm)_{PM}$ anomaly, and to increase the magnitude of the $(La/Sm)_{PM}$ anomaly over the plume (Fig. 9). Both Model 3.1 and 3.2 predict > 100% of the width and amplitude of the $^{87}Sr/^{86}Sr$ anomaly. The amplitudes of the $(La/Sm)_{PM}$ anomalies in Models 3.1 and 3.2 are ∼70% and 85% of that observed in median values near Iceland, respectively. The widths of the $(La/Sm)_{PM}$ anomalies in Models 3.1 and 3.2 are 340 km and 425 km. Thus, Model 3.2 predicts ∼90% of the lower-bound estimate of the width of the $(La/Sm)_{PM}$ anomaly observed at Iceland and ∼50% of the upper-bound estimate.

Alternatively, if instead of an increase in ϕ_{EC}/ϕ_{DC} within the plume core, we assume $^{DC}[Sr]_0$ decreases by 35%, or I^{DC} increases from 0.70220 to 0.7024 within the central core, the predicted $^{87}Sr/^{86}Sr$ along the ridge is nearly identical to the prediction of Model 3.1. These alternative possibilities simulate a depleted plume component that is distinct from the depleted upper mantle. Similarly, models in which $^{DC}[La]_0$ is increased by 150%, or $^{DC}[Sm]_0$

is decreased by 40% inside the plume core produce along-axis variations in $(La/Sm)_{PM}$ that are very similar to the predictions of Model 3.2. These alternatives are presented mostly for comparison, and may not be reasonable compositions of actual mantle components.

Whereas it is commonly thought that the Iceland plume contains more enriched material than ambient upper mantle, this work contributes a quantitative means of explaining the gradual decrease in the expression of enriched components relative to depleted components with distance away from the center of Iceland. We find that only a subtle difference between the average composition of the plume and ambient mantle is needed to explain geochemical variations near Iceland because gradients in mantle dynamics and melting cause along-axis geochemical variations even if the plume and ambient mantle have the same average composition. To explain what a "subtle difference" is, consider that when the central, "enriched" plume material of Model 3.1 is melted in a simple mid-ocean ridge setting (i.e., without the active plume upwelling) it produces a "normal" mid-ocean ridge basalt $^{87}Sr/^{86}Sr$ ratio of 0.70298, compared to the 0.70283 produced by melting the reference material in Model 3.1 at a mid-ocean ridge setting. Both compositions fall within one standard deviation about the median seen in "normal" mid-ocean ridge basalts globally (i.e., 0.7022–0.7030) (Ito and van Keken, 2007; Ito and Mahoney, 2005b). We thus question to what degree the source reservoir of the Iceland plume is necessarily different, in terms of its overall geochemical character, from the upper mantle feeding mid-ocean ridges globally. The model predictions support the possibility proposed by Ito and Mahoney (2005b, 2006) that the mantle need not be compositionally stratified to explain the compositional differences between the Earth's major hotspots and sections of mid-ocean ridges not influenced by hotspots.

5. Conclusions

We have predicted the composition of pooled magma rising from a uniformly veined, ridge-centered mantle plume, and found that upper mantle dynamics can cause substantial geographic variations in the composition of magma erupted along the ridge. Doing so requires at least two components that begin melting at different depths and that have different trace element and isotope ratios. Results show that the dynamics associated with the plume upwelling causes a short-wavelength high (≲ 800 km in full width) in the mass fraction of an enriched component (EC) in the pooled magma that is centered over the plume, assuming EC begins melting deepest. This local high is higher than anywhere else along the ridge if viscosity increases with the dehydration of olivine in hydrous peridotite during progressive melting. This short-wavelength compositional anomaly is surrounded by a long-wavelength anomaly with a relatively low contribution from EC. The long-wavelength anomaly is caused in part by plume spreading, which diminishes upwelling related to plate separation and transfers material that was partially depleted near the center of the plume laterally along the axis.

The long-wavelength anomaly marks the total along-axis "waist" width of plume influence, and is shown to increase linearly with the square root of buoyancy flux, B, which is consistent with previous studies of the plume–ridge interaction (Ribe et al., 1995). The short-wavelength high in EC is most relevant to many geochemical observations of plume-influenced ridges, and also is shown to increase with $B^{1/2}$, primarily because the short-wavelength anomaly is sensitive to the radius of the plume, rather than to the reference viscosity.
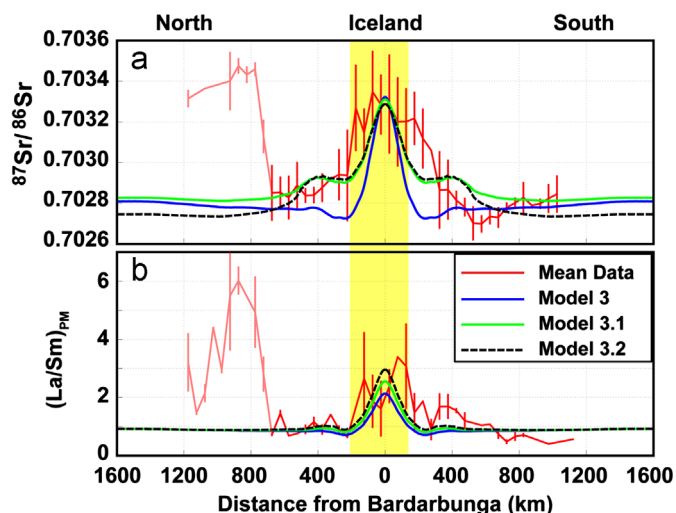
Fig. 9. (a) Median $^{87}Sr/^{86}Sr$ observed at Iceland (red line) and standard deviation about the mean for data grouped in 50 km intervals (as in Fig. 8a). Model 3 (blue line) as in Fig. 8 is plotted for reference. Models 3.1 (green line) and 3.2 (black, dashed line) have 3% and 6% less DC (by massfraction ϕ^{DC}) inside the plume core, respectively (see text for details). (b) $(La/Sm)_{PM}$ data and model predictions (as in Fig. 8c). Crustal thickness predictions for these models are indistinguishable from those of Model 3 (Fig. 8b). Yellow shading indicates the north–south extent of subaerial Iceland. (For interpretation of the references to color in this figure legend, the reader is referred to the web version of this article.)

We address the $^{87}Sr/^{86}Sr$, La/Sm, and crustal thickness variation along the MAR near Iceland. Our preferred model without any regional-scale compositional zoning (Model 3) simulates a plume radius that is consistent with mantle tomography. Model 3 predicts a peak in crustal thickness that is about 80% of that observed on Iceland accompanying local high in $^{87}Sr/^{86}Sr$ with an amplitude comparable to that of median compositions near Iceland. The main weaknesses of Model 3 are that it predicts a local high in La/Sm with amplitude that is ~38% of median compositions near Iceland, and it predicts narrower $^{87}Sr/^{86}Sr$ and La/Sm anomalies than those observed over Iceland.

Two cases are presented that are dynamically similar to Model 3, but in which compositional zoning is imposed in the form of the hottest interior of the rising plume being more "enriched" than the rest of the mantle. These two cases better predict the widths and amplitudes of $^{87}Sr/^{86}Sr$ and La/Sm anomalies near Iceland. In these cases, the bulk composition of the Icelandic plume is slightly different from that of the model ambient upper mantle, but not different from estimates of upper mantle typically sampled at normal ridges globally. This latter result motivates questions about the need for strong, large-scale stratification in mantle composition to explain observations near Iceland.

Acknowledgments

Appendix A. Supplementary material

Supplementary data associated with this article can be found in the online version at http://dx.doi.org/10.1016/j.epsl.2013.03.050.

References

Allen, R.M., Nolet, G., Morgan, W.J., Vogfjord, K., Bergsson, B.H., Erlendsson, P., Foulger, G.R., Jakobsdottir, S., Julian, B.R., Pritchard, M.J., Ragnarsson, S., Stefansson, R., 2002. Imaging the mantle beneath Iceland using integrated seismological techniques. J. Geophys. Res. 107, 2325, http://dx.doi.org/10.1029/2001JB000595.

Bianco, T.A., Ito, G., Becker, J.M., Garcia, M.O., 2005. Secondary Hawaiian volcanism formed by flexural arch decompression. Geochem. Geophys. Geosyst. 6, http://dx.doi.org/10.1029/2005GC000945.

Bianco, T.A., Ito, G., van Hunen, J., Ballmer, M.D., Mahoney, J.J., 2008. Geochemical variation at the Hawaiian hot spot caused by upper mantle dynamics and melting of a heterogeneous plume. Geochem. Geophys. Geosyst. 9, http://dx.doi.org/10.1029/2008GC0022111.

Bianco, T.A., Ito, G., van Hunen, J., Ballmer, M.D., Mahoney, J.J., 2011. Geochemical variations at intraplate hotspots caused by variable melting of a veined mantle plume. Geochem. Geophys. Geosyst. 12, Q0AC13, http://dx.doi.org/10.1029/2011GC003658.

Brown, J.W., White, R.S., 1994. Variation with spreading rate of oceanic crustal thickness and geochemistry. Earth Planet. Sci. Lett. 121, 435–449.

Breddam, K., 2002. Kistufell: primitive melting from Iceland mantle plume. J. Petrol. 43, 345–373.

Christensen, U., 1984. Convection with pressure- and temperature-dependent non-Newtonian rheology. Geophys. J. R. Astron. Soc. 77, 343–384.

Cohen, R.S., O'Nions, R.K., 1982. Identification of recycled continental material in the mantle from Sr, Nd, and Pb isotope investigations. Earth Planet. Sci. Lett. 61, 73–84.

Darbyshire, R., Bjarnason, I.T., White, R.S., Flovenz, O., 1998. Crustal structure above the Iceland mantle plume imaged by the ICEMELT refraction profile. Geophys. J. Int. 13, 1131–1149.

Davis, E.E., Lister, C.R.B., 1974. Fundamentals of ridge crest topography. Earth Planet. Sci. Lett. 21, 405–413, http://dx.doi.org/10.1016/0012-821X(74)90180-0.

DeMets, C., Gordon, R.G., Argus, D.F., 2010. Geologically current plate motions. Geophys. J. Int. 181, 1–80, http://dx.doi.org/10.1111/j.1365-246X.2009.04491.x.

Dick, H., Lin, J., Schouten, H., 2003. An ultraslow-spreading class of ocean ridge. Nature 426, 405–412, http://dx.doi.org/10.1038/nature.02128.

Elliot, T.R., Hawkesworth, C.J., Gronvöld, K., 1991. Dynamic melting of the Iceland plume. Nature 351, 201–206.

Farnetani, C.G., Richards, M.A., 1995. Thermal entrainment and melting in mantle plumes. Earth Planet. Sci. Lett. 133, 251–267.

Feighner, M.A., Richards, M.A., 1995. The fluid dynamics of plume–ridge and plume–plate interactions: an experimental investigation. Earth Planet. Sci. Lett. 129, 171–182.

Fitton, J.G., Saunder, A., Norry, M., Hardson, B.S., Taylor, R.N., 1997. Thermal and chemical structure of the Iceland plume. Earth Planet. Sci. Lett. 153, 197–208.

Hanan, B.B., Blichert-Toft, J., Kingsley, R.H., Schilling, J.-G., 2000. Depleted Iceland mantle plume geochemical signature: aritifact of multicomponent mixing? Geochem. Geophys. Geosyst. 1, http://dx.doi.org/10.1029/1999GC000009.

Hanan, B.B., Schilling, J.-G., 1997. The dynamic evolution of the Iceland mantle plume: the lead isotope perspective. Earth Planet. Sci. Lett. 151, 43–60.

Hards, V.L., Kempton, P.D., Thompson, R.N., 1995. The heterogeneous Iceland plume —new insights from the alkaline basalts of the Snaefell volcanic center. J. Geol. Soc. London 152, 1003–1009.

Hart, S.R., Schilling, J.-G., Powell, J.L., 1973. Basalts from Iceland and along the Reykjanes Ridge: Sr isotope geochemistry. Nat. Phys. Sci. 246, 104–107.

Hauri, E.H., Whitehead, J.A., Hart, S.R., 1994. Fluid dynamics and geochemical aspects of entrainment in mantle plumes. J. Geophys. Res. 99, 24275–24300.

Hemond, C., Condomines, M., Fourcade, S., Allegre, C.J., Oskarsson, N., Javoy, M., 1988. Thorium, strontium and oxygen isotope geochemistry in recent tholeiites from Iceland: crustal influence on mantle-derived magmas. Earth Planet. Sci. Lett. 87, 273–285.

Hemond, C.N.T.Arndt, Lichtenstein, U., Hofmann, A.W., Oskarsson, N., Steinthorsson, S., 1993. The heterogeneous Iceland plume: Nd–Sr–O isotopes and trace element constraints. J. Geophys. Res. 98, 15833–15850.

Herzberg, C., Asimow, P.D., Arndt, N., Niu, Y., Lesher, C.M., Fitton, J.G., Cheadle, M.J., Saunders, A.D., 2007. Temperatures in ambient mantle and plumes: constraints from basalts, picrites, and komatiites. Geochem. Geophys. Geosyst. 8 (2), Q02006.

Hirth, G., Kohlstedt, D.L., 1996. Water in the oceanic upper mantle: implications for rheology, melt extraction and the evolution of the lithosphere. Earth Planet. Sci. Lett. 144, 93–108.

Hirth, G., Kohlstedt, D.L., 2003. Rheology of the upper mantle and the mantle wedge: a view from the experimentalists, Inside the subduction factory. In: Eiler, J. (Ed.), Geophysical Monograph 138. American Geophysical Union, Washington, DC, pp. 83–105.

Hooft, E.E., Brandsdottir, B., Mjelde, R., Shimamura, H., Murai, Y., 2006. Asymmetric plume–ridge interaction around Iceland: the Kolbeinsey Ridge Iceland Seismic Experiment. Geochem. Geophys. Geosyst. 7, http://dx.doi.org/10.1029/2005GC001123.

Hung, S.-H., Shen, Y., Chiao, L.-Y., 2004. Imaging seismic velocity structure beneath the Iceland hot spot: a finite frequency approach. J. Geophys. Res. 109, 8305–8321.

Ingle, S., Ito, G., Mahoney, J.J., Chazey III, W., Sinton, J., Rotella, M., Christie, D.M., 2010. Mechanisms of geochemical and geophysical variations along the western Galapagos Spreading Center, Geochem. Geophys. Geosyst. 11, Q04003, http://dx.doi.org/10.1029/2009GC002694.

Ito, G., Bianco, T. Patterns in Galapagos magmatism arising from the upper mantle dynamics of plume–ridge interaction. In: d'Ozouville, N., Graham, D., Harpp, K.S., Mittelstaedt, E. (Eds.), The Galapagos: An Earth Science Laboratory. AGU Geophysical Monograph Series, Washington, DC, in press.

Ito, G., Lin, J., Graham, D., 2003. Observational and theoretical studies of the dynamics of mantle plume-mid-ocean ridge interaction. Rev. Geophys. 41, 1017–1041, http://dx.doi.org/10.1029/2002RG000117.

Ito, G., Mahoney, J.J., 2005a. Flow and melting of a heterogeneous mantle: 1. Method and importance to the geochemistry of ocean island and mid-ocean ridge basalts. Earth Planet. Sci. Lett. 230, 29–46, http://dx.doi.org/10.1016/j.epsl.2004.10.035.

Ito, G., Mahoney, J.J., 2005b. Flow and melting of a heterogeneous mantle: 2. Implications for a chemically nonlayered mantle. Earth Planet. Sci. Lett. 230, 47–63, http://dx.doi.org/10.1016/j.epsl.2004.10.034.

Ito, G., Mahoney, J.J., 2006. Melting a high $^3He/^4He$ source in a heterogeneous mantle. Geochem. Geophys. Geosyst. 7, http://dx.doi.org/10.1029/2005GC001158.

Ito, G., Shen, Y., Hirth, G., Wolfe, C., 1999. Mantle flow and dehydration of the Iceland mantle plume. Earth Planet. Sci. Lett. 165, 81–96.

Ito, G., van Keken, P.E., 2007. Hot spots and melting anomalies. In: Bercovici, D. (Ed.), Mantle Dynamics, Treatise in Geophysics, vol. 7. Elsevier, pp. 371–435.

Jackson, M.G., Hart, S.R., Koppers, A.A.P., Hubert, S., Konter, J., Blusztajn, J., Kurz, M., Russell, J.A., 2007. The return of subducted continental crust in Samoan lavas. Nature 448, 684–687, http://dx.doi.org/10.1038/nature06048.

Johnson, K., Dick, H., Shimizu, N., 1990. Melting in the oceanic upper mantle: an ion microprobe study of diopsides in abyssal peridotites. J. Geophys. Res. 95, 2661–2678.

Katz, R.F., Spiegelman, M., Langmuir, C.H., 2003. A new parameterization of hydrous mantle melting. Geochem. Geophys. Geosyst. 4, http://dx.doi.org/10.1029/2002GC000433.

Kelemen, P.B., Hirth, G., Shimizu, N., Spiegelman, M., Dick, H.J.B., 1997. A review of melt migration processes in the asthenospheric mantle beneath oceanic spreading centers. Philos. Trans. R. Soc. London 355, 283–318.

Kokfelt, T.F., Hoernle, K., Hauff, F., Fiebig, J., Werner, R., Garbe-Schonberg, D., 2006. Combined trace element and Pb–Nd–Sr–O isotope evidence for recycled oceanic crust (upper and lower) in the Iceland mantle plume. J. Petrol. 47, 1705–1749, http://dx.doi.org/10.1093/petrology/eg1025.

Lee, C.-T.A., Luffi, P., Plank, T., Dalton, H., Leeman, W.P., 2009. Constraints on the depths and temperatures of basaltic magma generation on Earth and other terrestrial planets using new thermobarometers for mafic magmas. Earth Planet. Sci. Lett. 279, 20–33.

Lyubetskaya, T., Korenaga, J., 2007. Chemical composition of Earth's primitive mantle and its variance: 1. Method and results. J. Geophys. Res. 112, B03211, http://dx.doi.org/10.1029/2005JB004223.

Maclennan, J.D., McKenzie, Gronvöld, K., 2001. Plume-driven upwelling under central Iceland. Earth Planet. Sci. Lett. 194, 67–82.

McKenzie, D., 2000. Constraints on melt generation and transport from U-series activity ratios. Chem. Geol. 162, 81–94.

McKenzie, D., O'Nions, R.K., 1991. Partial melt distribution from inversion of rare earth element concentrations. J. Petrol. 32, 1021–1091.

Menke, W., 1999. Crustal isostasy indicates anomalous densities beneath Iceland. Geophys. Res. Lett. 26, 1215–1218.

Mertz, D.F., Devey, C.W., Todt, W., Stoffers, P., Hofmann, A.W., 1991. Sr–Nd–Pb isotope evidence against plume–asthenosphere mixing north of Iceland. Earth Planet. Sci. Lett. 107, 243–255.

Mertz, D.F., Haase, K.M., 1997. The radiogenic isotope composition of the high-latitude North Atlantic mantle. Geology 25, 411–414.

Michael, P., 1995. Regionally distinctive sources of depleted MORB: evidence from trace elements and H_2O. Earth Planet. Sci. Lett. 131, 301–320.

Moresi, L., Gurnis, M., 1996. Constraints on the lateral strength of slabs from three-dimensional dynamic flow models. Earth Planet. Sci. Lett. 138, 15–28.

Morgan, W.J., 1972. Deep mantle convection plumes and plate motions. Am. Assoc. Pet. Geol. Bull. 56, 203–213.

Murton, B.J., Taylor, R.N., Thirlwall, M.F., 2002. Plume–ridge interaction: a geochemical perspective from the Reykjanes Ridge. J. Petrol. 43, 1987–2012, http://dx.doi.org/10.1093/petrology/43.11.1987.

O'Nions, R.K., Parkhurst, R.J., 1974. Petrogenetic significance of isotope and trace element variations in volcanic rocks from the Mid-Atlantic. J. Petrol. 15, 603–634.

O'Nions, R.K., Parkhurst, R.J., Fridleifsson, I.B., Jakobsson, P., 1973. Strontium isotopes and rare earth elements in basalts from Heimay and Surstey volcanic eruptions. Nature 243, 213–214.

O'Nions, R.K., Parkhurst, R.J., Gronvöld, K., 1976. Nature and development of basalt magma sources beneath Iceland and the Reykjanes Ridge. J. Petrol. 17, 315–338.

Peate, D.W., Hawkesworth, C.J., van Calsteren, P.W., Taylor, R.N., Murton, B.J., 2001. $^{238}U–^{230}Th$ constraints on mantle upwelling and plume–ridge interaction along the Reykjanes Ridge. Earth Planet. Sci. Lett. 187, 259–272.

Putirka, K.D., 2005. Mantle potential temperatures at Hawaii, Iceland, and the mid-ocean ridge system, as inferred from olivine phenocrysts: evidence for thermally driven mantle plumes. Geochem. Geophys. Geosyst. 6, Q05L08, http://dx.doi.org/10.1029/2005GC000915.

Ribe, N.M., Christensen, U.R., Theiing, J., 1995. The dynamics of plume–ridge interaction, 1: Ridge-centered plumes. Earth Planet. Sci. Lett. 134, 155–168.

Rubin, K.H., van der Zander, I., Smith, M.C., Bergmanis, E.C., 2005. Minimum speed limit for ocean ridge magmatism from $^{210}Pb–^{226}Ra–^{230}Th$ disequilibria. Nature 437, 534–538, http://dx.doi.org/10.1038/nature03993.

Salters, V.J.M., Stracke, A., 2004. Composition of the depleted mantle. Geochem. Geophys. Geosyst. 5 (5), Q05004.

Schilling, J.-G., 1973. Iceland mantle plume: geochemical study of Reykjanes Ridge. Nature 242, 565–571, http://dx.doi.org/10.1038/242565a0.

Schilling, J.G., 1991. Fluxes and excess temperatures of mantle plumes inferred from their interaction with migrating mid-ocean ridges. Nature 352, 397–403.

Schilling, J.-G., Zajac, M., Evans, R., Johnston, T., White, W., Devine, J.D., Kingsley, R., 1983. Petrologic and geochemical variations along the Mid-Atlantic Ridge from 29°N to 73°N. Am. J. Sci. 283, 510–586.

Schilling, J.-G., Kingsley, R.H., Fontingnie, D., Poreda, R., Xue, S., 1999. Dispersion of the Jan Mayen and Iceland mantle plumes in the Arctic: a He–Pb–Nd–Sr isotope tracer study of basalts from the Kolbeinsy, Mohns, and Knipovich Ridges. J. Geophys. Res. 104 (10), 543–10569.

Shaw, D.M., 1970. Trace element fractionation during anatexis. Geochim. Cosmochim. Acta 34, 237–243.

Sleep, N.H., 1990. Hotspots and mantle plumes: some phenomenology. J. Geophys. Res. 95, 6175–6736.

Smallwood, J.R., White, R.S., Minshull, T.A., 1995. Sea-floor spreading in the presence of the Iceland plume: the structure of the Reykjanes Ridge at 61°40′ N. J. Geol. Soc. London 152, 1023–1029.

Stecher, O., Carlson, R.W., Gunnarsson, B., 1999. Torfajökull: a radiogenic end-member of the Iceland Pb-isotopic array. Earth Planet. Sci. Lett. 165, 117–127.

Stracke, A., Zindler, A., Salters, V., McKenzie, D., Blichert-Toft, J., Albarede, F., Gronvöld, K., 2003. Theistareykir revisited. Geochem. Geophys. Geosyst. 4, http://dx.doi.org/10.1029/2001GC000201.

Stracke, A., Bourdon, B., McKenzie, D., 2006. Melt extraction in the Earth's mantle: constraints from U–Th–Pa–Ra studies in oceanic basalts. Earth Planet. Sci. Lett. 244, 97–112, http://dx.doi.org/10.1016/j.epsl.2006.01.057.

Sun, S.-S., Jahn, B.-M., 1975. Lead and strontium isotopes in post-glacial basalts from Iceland. Nature 255, 527–530.

Taylor, R.N., Thirlwall, M.F., Murton, B.J., Hilton, D.R., Gee, M.A.M., 1997. Isotopic constraints on the influence of the Icelandic plume. Earth Planet. Sci. Lett. 148, E1–E8, http://dx.doi.org/10.1016/S0012-821X(97)00038-1.

Thirlwall, M.F., Gee, M.A.M., Taylor, R.N., Murton, B.J., 2004. Mantle components in Iceland and adjacent ridges investigated using double-spike Pb isotope ratios. Geochim. Cosmochim. Acta 68, 361–386.

van Hunen, J., Zhong, S., Shapiro, N.M., Ritzwoller, M.H., 2005. New evidence for dislocation creep from 3-D geodynamic modeling of the Pacific upper mantle structure. Earth Planet. Sci. Lett. 238, 146–155, http://dx.doi.org/10.1016/j.epsl.2005.07.006.

Vogt, P.R., 1971. Asthenosphere motion recorded by the ocean floor south of Iceland. Earth Planet. Sci. Lett. 13, 153–160, http://dx.doi.org/10.1016/0012-821X(71)90118-X.

Watts, A.B., Zhong, S., 2000. Observations of flexure and rheology of oceanic lithosphere. Geophys. J. Int. 142, 855–875.

Weir, N., White, R.S., Brandsdottir, B., Einarsson, P., Shimamura, H., Shiobara, H., 2001. Crustal structure of the northern Reykjanes Ridge and Reykjanes Peninsula, south-west Iceland. J. Geophys. Res. 106, 6347–6368.

White, R.S., McKenzie, D., O'Nions, R.K., 1992. Oceanic crustal thickness from seismic measurements and rare earth element inversions. J. Geophys. Res. 97, 19683–19715.

White, W.M., Schilling, J.-G., 1978. The nature and origin of geochemical variation in Mid-Atlantic Ridge basalts from the Central North Atlantic. Geochim. Cosmochim. Acta 42, 1501–1516.

Willbold, M., Stracke, A., 2006. Trace element composition of mantle end-members: implications for recycling of oceanic and upper and lower continental crust. Geochem. Geophys. Geosyst. 7 (4), Q04004.

Wilson, J.T., 1963. A possible origin of the Hawaiian Islands. Can. J. Phys. 41, 863–870.

Wolfe, C., Bjarnason, I.T., VanDecar, J.C., Solomon, S.C., 1997. Seismic structure of the Iceland mantle plume. Nature 385, 245–247.

Wood, D.A., Joron, J.-L., Treuil, M., Norry, M., Tarney, J., 1979. Elemental and Sr isotope variations in basic lavas from Iceland and the surrounding ocean floor: the nature of mantle source inhomogeneities. Contrib. Mineral. Petrol. 70, 319–329.

Zhong, S., Zuber, M.T., Moresi, L., Gurnis, M., 2000. Role of temperature-dependent viscosity and surface plates in spherical shell models of mantle convection. J. Geophys. Res. 105, 11063–11082.

Zhu, W., Gaetani, G.A., Fusseis, F., Montesi, L.G., De Carlo, F., 2011. Microtomography of partially molten rocks: three-dimensional melt distribution in mantle peridotite. Science 332, 88–91, http://dx.doi.org/10.1126/science.1202221.

Zindler, A., Hart, S.R., Frey, F.A., Jakobsson, S.P., 1979. Nd and Sr isotope rations and rare earth element abundances in Reykjanes Peninsula basalts: evidence for mantle heterogeneity beneath Iceland. Earth Planet. Sci. Lett. 45, 249–262.